CO_2 Dissolution Trapping Rates in Heterogeneous Porous Media

K. A. Gilmore[1], J. A. Neufeld[1,2,3], M. J. Bickle[4]

[1]Bullard Laboratories, Department of Earth Sciences, University of Cambridge, Madingley Rise, Madingley Road, Cambridge, CB3 0EZ, UK
[2]BP Institute, University of Cambridge, Madingley Road, Cambridge, CB3 0EZ, UK
[3]Institute of Theoretical Geophysics, Department of Applied Mathematics and Theoretical Physics, University of Cambridge, Cambridge, CB3 0WA, UK
[4]Department of Earth Sciences, University of Cambridge, Downing Street, Cambridge, CB2 3EQ, UK

Key Points:

- Injection of carbon dioxide into finely bedded reservoirs leads to enhanced contact area with water and hence enhanced dissolution rates.
- Propagation rates of free-phase carbon dioxide transition from advection to diffusion dominated as the contact area with water increases.
- For injection into the Salt Creek reservoir, Wyoming, nearly 10% of the injected carbon dioxide is predicted to dissolve in one year.

Corresponding author: Kieran Gilmore, kg382@cam.ac.uk

This article has been accepted for publication and undergone full peer review but has not been through the copyediting, typesetting, pagination and proofreading process which may lead to differences between this version and the Version of Record. Please cite this article as doi: 10.1029/2020GL087001

Abstract

The rate of carbon dioxide (CO_2) dissolution in saline aquifers is the least well-constrained of the secondary trapping mechanisms enhancing the long-term security of geological carbon storage. CO_2 injected into a heterogeneous saline reservoir will preferentially travel along high permeability layers increasing the CO_2-water interfacial area which increases dissolution rates. We provide a conservative, first-principles analysis of the quantity of CO_2 dissolved and the rate at which free-phase CO_2 propagates in layered reservoirs. At early times, advection dominates the propagation of CO_2. This transitions to diffusion dominated propagation as the interfacial area increases and diffusive loss slows propagation. As surrounding water-filled layers become CO_2 saturated, propagation becomes advection dominated. For reservoirs with finely bedded strata, $\sim$10% of the injected CO_2 can dissolve in a year. The maximum fraction of CO_2 that dissolves is determined by the volumetric ratio of water in low permeability layers and CO_2 in high permeability layers.

Plain Language Summary

To limit global warming to 2°C, it is likely that large amounts of carbon dioxide (CO_2) will need to be stored underground. A significant fraction of the total possible storage space for CO_2 is in salt water reservoirs, kilometers beneath the surface. It is important that once the CO_2 has been injected underground it is securely trapped, otherwise there is a risk that it could leak back to the surface. After the CO_2 is injected into these reservoirs it can dissolve in the surrounding water, greatly reducing the risk of leakage, although complete dissolution of all the injected CO_2 may take millions of years. However, preferential flow of CO_2 along more permeable layers in geological formations creates a complex front between the water and CO_2 which increases the surface area available for dissolution. This study calculates the minimum amount of injected CO_2 that can dissolve in such a reservoir, and how far it travels. Using injection of CO_2 for enhanced oil recovery at the Salt Creek Field in Wyoming as an example, we find that in one year around 10% of the total injected CO_2 can dissolve into the surrounding water by this process and become trapped.

1 Introduction

Worldwide carbon dioxide (CO_2) emission targets are unlikely to be met without large scale geological CO_2 storage (Intergovernmental Panel on Climate Change, 2018). Assessments of global CO_2 storage capacity (e.g. Michael et al. (2010)) suggest that saline aquifers could account for around 90% of the total potential storage volume. The dissolution of injected CO_2 into the ambient brine within a saline aquifer is a key mechanism for increasing the security of long-term storage. At typical storage reservoir conditions, CO_2 is in the supercritical phase and is buoyant with respect to the surrounding reservoir fluid, presenting the risk of migration to the surface. As CO_2 dissolves into water the density of the water increases (Teng & Yamasaki, 1998), eliminating the buoyancy of free-phase CO_2 and reducing the risk of leakage. Quantifying total dissolution rates post injection is therefore important for assessing the contribution of CO_2 dissolution to the long-term security of stored CO_2.

The rate of CO_2 dissolution in formation waters is controlled by the diffusive transport of dissolved CO_2 away from the CO_2-water contact and the area of the contact. Because diffusive fluxes into a static system decrease as the square-root of time and the CO_2 diffusion coefficient is small ($\sim 2\times10^{-9}$ m^2s^{-1} (Cadogan et al., 2014)), CO_2-enriched boundary layers in water in contact with free-phase CO_2 (Lindeberg & Wessel-Berg, 1997) will grow to $\sim$10 cm thick in 1 year or $\sim$1 m in 100 years. The relative movement of water and CO_2 will therefore exert an important control on CO_2 dissolution rates. Dur-

ing injection and flow, the lower viscosity of the CO_2 will result in fingering (Saffman & Taylor, 1958) which will be strongly enhanced by reservoir heterogeneities. It is the resulting complexities in the geometry of the CO_2-water interface and flow of CO_2 that makes CO_2 dissolution difficult to quantify.

There are few constraints on CO_2 dissolution during CO_2 injection. Measurements of $CO_2/^3He$ ratios show that some natural CO_2 accumulations have lost more than 90% of their original CO_2 by dissolution over hundreds of thousands to millions of years (Gilfillan et al., 2009). At Green River, Utah, where natural CO_2 has been migrating up a fault system for several hundred thousand years, Bickle and Kampman (2013) estimated that less than 1% of the CO_2 escaped to the surface, the rest being dissolved in permeable horizons intersected by the fault system. Most modelling of CO_2 dissolution has concentrated on the impact of convective circulation of the brine beneath CO_2 accumulations driven by the density increase as brine saturates with CO_2 (e.g. Ennis-King and Paterson (2005); Neufeld et al. (2010)). However, the marked anisotropy of permeabilities in most reservoirs substantially reduces the convective circulation (Green & Ennis-King, 2014). Reservoir simulations using numerical models typically use grid sizes of more than 10 m which are unable to model flow heterogeneities on length scales of ∼1 m or less over which diffusion dominates. There are limited constraints on dissolution rates from measurements on small-scale injection experiments. In the Frio experiment, Texas, Freifeld et al. (2005) noted that the arrival times of the tracer krypton lagged the arrival of the tracers sulfur hexafluoride and perfluorocarbon and attributed this to the higher solubility of krypton in brine. Likewise Lu et al. (2012) observed a similar lag between sulfur hexafluoride and kyrpton tracers in the Cranfield, Mississippi CO_2 injection experiment. However, attempts to quantify such observations have had limited success (e.g. LaForce et al. (2014)). In a CO_2 injection phase at the Salt Creek, Wyoming enhanced oil recovery site, Bickle et al. (2017) observed that dissolution of CO_2 in formation brines drove significant reactions with silicate minerals, but again the difficulty in modelling the complex flows in a heterogeneous reservoir have so far precluded quantitative estimates.

The CO_2-brine interactions which determine CO_2 dissolution will be controlled by the reservoir heterogeneities on all scales and these are difficult to model properly, both because it is not possible to determine the reservoir structure at the sub-metre scales which matter for the diffusive processes, and because numerical models of CO_2 and brine flows in reservoirs are not currently capable of running at such resolutions. In this paper, we consider dissolution during CO_2 injection into a simple representation of a layered reservoir, and quantify the increased dissolution rates due to an increase in interfacial area between the CO_2 and the reservoir fluid. This provides a base case, given that the additional complexities are likely to substantially increase dissolution rates. The model is then evaluated using parameters appropriate to large-scale CO_2 injection such as reservoir bedding thickness, porosity, saturation and injection flux.

We model a horizontally layered reservoir comprising alternating higher and lower permeability layers. Free-phase, low viscosity CO_2 flow will preferentially be confined to the higher permeability layers. This will be enhanced by capillary entry pressures which impede CO_2 entering the lower permeability layers (c.f. Sathaye et al. (2014)). The model assumes horizontal strata within the reservoir with CO_2 flow confined to the high permeability layers and ignores buoyancy of the supercritical CO_2. It is assumed that there is no flow of CO_2 between layers, but there is diffusive exchange of CO_2 across the static, water-filled low permeability layers. The modelling provides a minimum estimate for CO_2 dissolution against which the effect of additional processes or field observations may be assessed. Mixing of CO_2 and water along formation boundaries, fingering of low viscosity CO_2 into formation waters and the consequent dissolution of CO_2 ahead of the CO_2 finger, and the much more complex permeability structures in most sedimentary rocks would all be expected to enhance dissolution rates, most probably by an order-of-magnitude

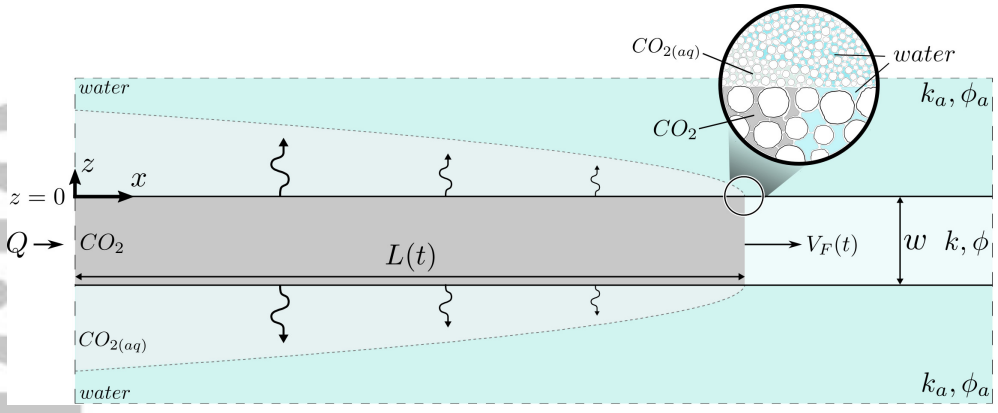

Figure 1. Schematic diagram of a two dimensional finger of free-phase CO_2 propagating along a high permeability porous layer that is initially saturated with water surrounded by a low permeability porous aquifer also saturated with water.

or more. It will likely only be possible to estimate the impact of these processes by experiments in field settings.

2 CO_2 Flow in a Single High Permeability Layer

2.1 Single Layer Model

We first consider CO_2 propagating along a single, high permeability layer of width w, porosity ϕ and permeability k in a low permeability, water saturated aquifer of porosity ϕ_a and permeability k_a (Figure 1). CO_2 is injected into the high permeability layer at constant volumetric rate Q. For simplicity, we assume that a finite capillary entry pressure confines the flow of free-phase CO_2 to the high permeability layer. The CO_2 finger has a total length $L(t)$ the front moves with a flux $V_F(t)$. The length of the CO_2 finger is much greater than its width so dissolution across the CO_2-water interface at the finger front is neglected and the interface is modelled as planar for simplicity.

The diffusive CO_2 profile away from the CO_2-water interface (in the z direction) for a given value of x is given by the solution for diffusion into a semi-infinite layer (Carslaw and Jaeger (1959), p. 59),

$$c = c_0 \operatorname{erfc}\left(\frac{z}{2\sqrt{D(t-t_0)}}\right), \tag{1}$$

where erfc is the complimentary error function, c_0 is the maximum solubility of CO_2 in water, t is the time since injection commenced and t_0 is the time at which the front passes position $x = L(t_0)$. The effective diffusion coefficient of CO_2 in water is given by

$$D = D_m \frac{\phi_a}{\tau}, \tag{2}$$

where D_m is the molecular diffusion coefficient of CO_2 in water and ϕ_a and τ are the porosity and tortuosity of the low permeability layer (Pismen, 1974).

The vertical CO_2 concentration gradient in the water is therefore

$$\frac{\partial c}{\partial z} = -\frac{c_0}{\sqrt{\pi D(t-t_0)}} \exp\left[\frac{-z^2}{4D(t-t_0)}\right], \tag{3}$$

and hence the vertical diffusive flux of CO_2 out of the high permeability layer at time t is,

$$F_{total}(t) \;=\; -2\phi_a \int_0^{L(t)} D\frac{dc}{dz}\Big|_{z=0} dx \;=\; 2\phi_a \int_0^{L(t)} c_0 \sqrt{\frac{D}{\pi(t-t_0)}}\, dx, \tag{4}$$

with ϕ_a introduced as CO_2 only diffuses into water within the pores. As a non-wetting phase, CO_2 only partially displaces water in the high permeability layer. This reduces the fraction of the porosity occupied by CO_2 (s_{nw}), and some CO_2 dissolves in the water occupying the remaining pore space.

The velocity of the CO_2 front at $x = L(t)$ is a function of the input flux and diffusive losses given by lateral diffusion from the finger and complete saturation of the residual water within the CO_2 finger,

$$V_F(t) = vw\phi s_{nw} = v_0 w\phi s_{nw} - 2\phi_a \int_0^{L(t)} c_0 \sqrt{\frac{D}{\pi(t-t_0)}}\, dx - vw\phi c_0(1-s_{nw}). \tag{5}$$

Here v is the interstitial velocity of CO_2 at the front and v_0 is the CO_2 interstitial velocity at $x = 0$. By introducing the non-dimensional variables

$$\tilde{v} = \frac{v}{v_0},\; \tilde{c} = \frac{c}{c_0},\; \tilde{x} = \frac{x c_0^2 \phi_a^2 D}{v_0 w^2 \phi^2 s_{nw}^2},\; \tilde{t} = \frac{t c_0^2 \phi_a^2 D}{w^2 \phi^2 s_{nw}^2}, \tag{6}$$

equation (5) may be rewritten in the generic form

$$(1+\alpha)\tilde{v} = 1 - 2\int_0^{\tilde{L}(\tilde{t})} \sqrt{\frac{1}{\pi(\tilde{t}-\tilde{t_0})}}\, d\tilde{x}, \tag{7}$$

where $\alpha = c_0(1-s_{nw})/s_{nw}$ is a measure of how much CO_2 dissolves into residual water within the CO_2 finger. Equation (7) gives the dimensionless front velocity as a function of dimensionless time. For notational convenience, we drop the '$\sim$' from all subsequent quantities. We solve equation (7) numerically using a sequential iteration approach. The CO_2 concentration gradient at the interface is calculated every timestep allowing the total diffusive flux to be deducted from the input flux giving the CO_2 velocity, v, as a function of time. The new front velocity allows the position of the CO_2 front, $L(t)$, to be calculated for the next timestep.

2.2 Results

Figure 2a illustrates the length of the CO_2 finger as a function of time. The length of the finger is governed by the input flux and the amount of dissolution. At early times ($t \ll 1$), when the dissolution area to input flux ratio of the CO_2 finger is small, the amount of dissolution is negligible and so the length evolves as $L \sim t$. The diffusive CO_2 profile away from the CO_2-water interface scales as $t^{-1/2}$, hence the total diffusive flux scales as $t^{1/2}$. The total dissolution into the low permeability layers is the sum of the total flux over time and so scales as $t^{3/2}$ (see supplementary material for graphs of dissolution scaling).

At late times ($t \gg 1$), the finger length evolves as $L \sim t^{1/2}$ as diffusive loss dominates. This means that the total diffusive flux tends towards a constant and hence the total dissolution evolves proportional to t. The transition between these two regimes happens when L and t are of the order one. Figure 2b shows the fraction of injected CO_2 lost by dissolution as a function of time. This fraction increases with time as the increase in the surface area increases the ratio of diffusive loss to input flux and tends to one as $t \to \infty$.

Figure 2 has been plotted for three values of α. When $\alpha = 0$, there is no dissolution into residual water in the CO_2 finger. At low values of α, the fraction of CO_2 dissolved in the residual water within the CO_2 finger is small compared with lateral loss

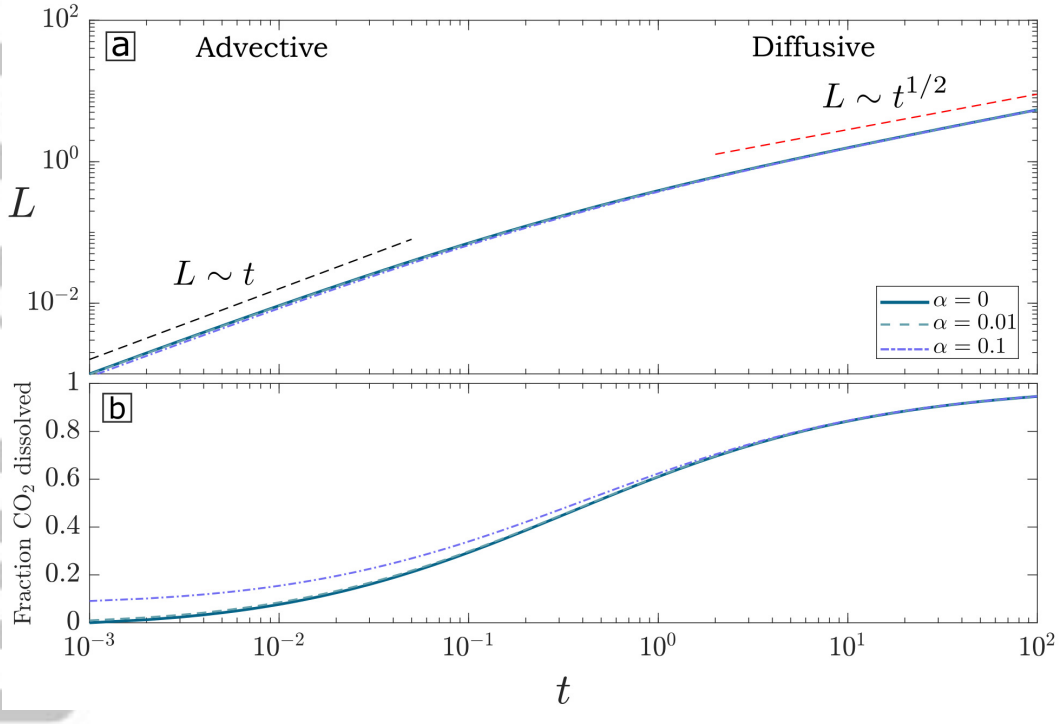

Figure 2. (a) Length of the CO_2 finger L as a function of time t. Also plotted is the line $L \sim t$ (black dashed line), and the tangent at long times, $L \sim t^{1/2}$ (red dashed line). (b) Fraction of CO_2 dissolved as a function of time. The fraction of CO_2 dissolved is the fraction of the total CO_2 injected into the system that has diffused into the surrounding water and saturated the residual water within the CO_2 finger. Both graphs are plotted for $\alpha = 0$, 0.01, 0.1.

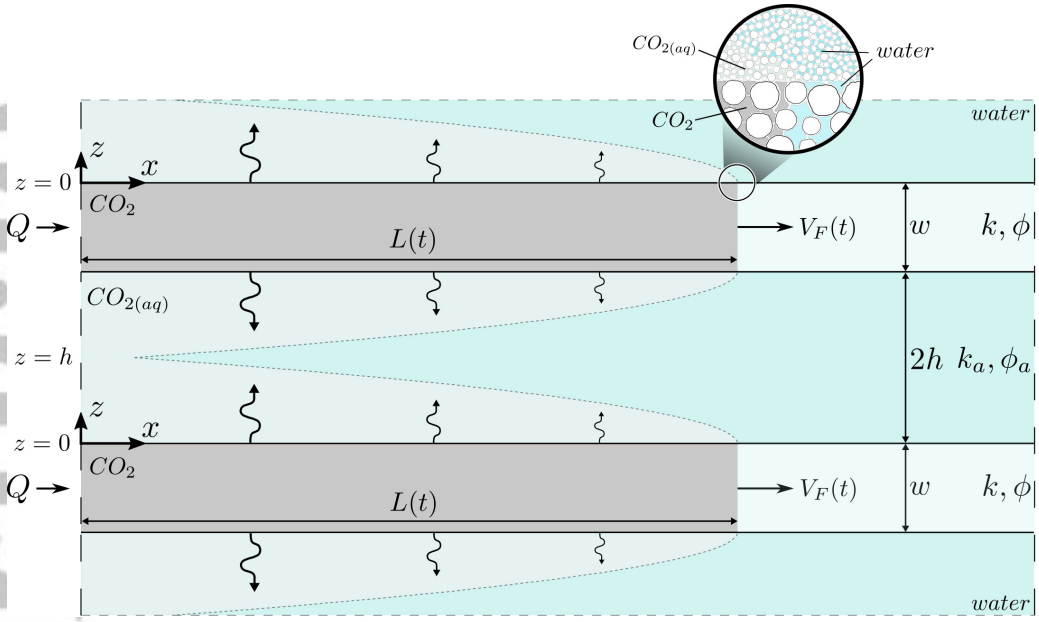

Figure 3. Schematic diagram of periodically repeating high permeability porous layers of width w, separated by low permeability porous layers of width, $2h$. The reservoir is initially saturated with water. CO_2 is injected into the high permeability layers. $z = 0$ at the high/low permeability interface and $z =$ h at the midpoint between the high permeability layers.

to the surrounding water. For a typical reservoir $\alpha = 0.014$ if $s_{nw} = 0.8$ (Krevor et al., 2015) and $c_0 = 5.5$ $wt\%$ (Dubacq et al., 2013).

3 CO_2 Flow Along Periodic High Permeability Layers

3.1 Multilayered Model

The saline aquifers suitable for geological storage are characteristically sandstones bedded on 10^{-2} to 1 meter scales with permeabilities that vary by an order of magnitude or greater. Injection of CO_2 will primarily occupy the high permeability layers and the diffusive fringes about the CO_2-filled layers will overlap. We illustrate this behaviour with a periodically layered reservoir with high permeability layers of width w, porosity ϕ and permeability k interbedded with low permeability layers of width $2h$, porosity ϕ_a and permeability k_a. CO_2 flows into each of the high permeability layers at volumetric rate Q. We assume that a finite capillary entry pressure confines advective flow of free-phase CO_2 to the high permeability layers (see figure 3). The diffusive profile between layers is given by the solution for diffusion into a layer bounded by two parallel planes (Carslaw and Jaeger (1959), p. 100),

$$c = c_0 - \frac{4c_0}{\pi}\sum_{n=0}^{\infty}\frac{(-1)^n}{2n+1}\exp\left[\frac{-D(2n+1)^2\pi^2(t-t_0)}{4h^2}\right]\cos\left[\frac{(2n+1)\pi(1-\frac{z}{h})}{2}\right]. \quad (8)$$

The velocity of the CO_2 front at $x = L$ is a function of the input flux, lateral diffusive loss and saturation of the residual water,

$$V_F(t) = vw\phi s_{nw} =$$
$$v_0 w\phi s_{nw} - \frac{4\phi_a c_0 D}{h}\int_0^{L(t)}\sum_{n=0}^{\infty}\exp\left[\frac{-D(2n+1)^2\pi^2(t-t_0)}{4h^2}\right]dx \; - \; vw\phi c_0(1-s_{nw}). \quad (9)$$

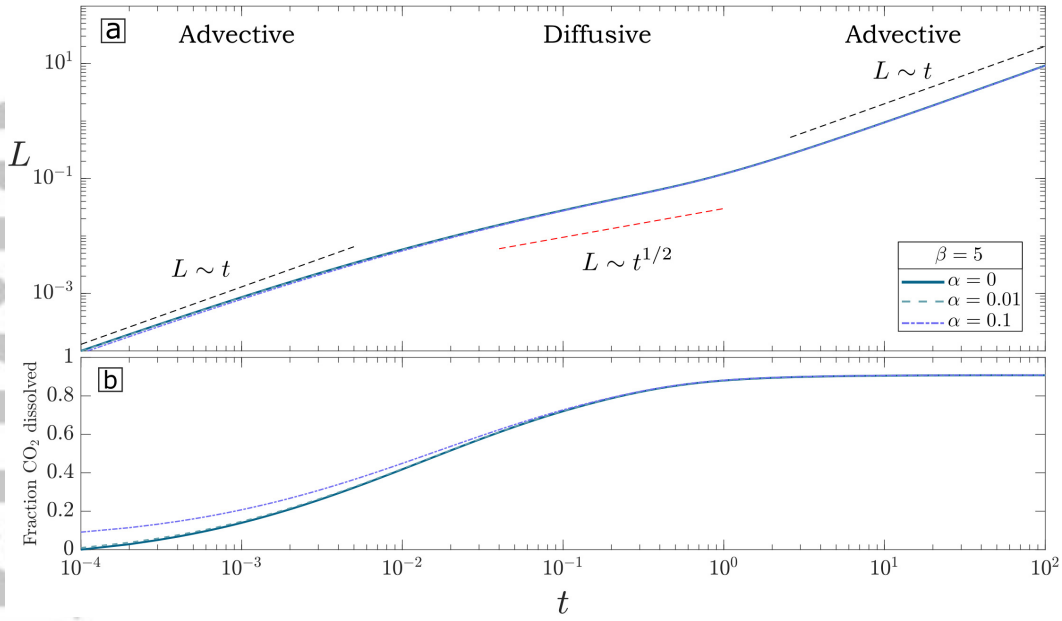

Figure 4. (a) Length of the CO_2 fingers L as a function of time t. Also plotted is the line $L \sim t$ (black dashed line), and the line $L \sim t^{1/2}$ (red dashed line). The length of the fingers increase as a linear function of t at both early and late times but with $L \sim t^{1/2}$ at intermediate times. (b) Fraction of CO_2 dissolved as a function of time. Both graphs plotted for $\beta = 5$ and $\alpha = 0$, 0.01, 0.1.

Introducing the non-dimensional variables

$$\tilde{v} = \frac{v}{v_0},\ \tilde{c} = \frac{c}{c_0},\ \tilde{x} = \frac{xD}{v_0 h^2},\ \tilde{t} = \frac{tD}{h^2},\ \tilde{z} = \frac{z}{h}, \tag{10}$$

equation (9) can be rewritten as

$$(1+\alpha)\tilde{v} = 1 - 4\beta \int_0^{\tilde{L}(\tilde{t})} \sum_{n=0}^{\infty} \exp\left[\frac{-(2n+1)^2\pi^2(\tilde{t}-\tilde{t_0})}{4}\right] d\tilde{x}\ , \tag{11}$$

where $\alpha = c_0(1-s_{nw})/s_{nw}$ and $\beta = \frac{h\phi_a c_0}{w\phi s_{nw}}$. For notational convenience, we drop the '$\sim$' from all subsequent quantities. A similar iterative solution to the single finger case is used to solve equation (11) to give the CO_2 front position and velocity, and total dissolution of CO_2 as a function of time for the multi-layered model.

3.2 Results

Figure 4a illustrates the length of the CO_2 fingers as a function of time for $\beta = 5$ and three values of α. The length of the fingers evolve in three stages. At early times ($t \ll 1$) the length of the fingers evolve as $L \sim t$, at intermediate times they evolve as $L \sim t^{1/2}$, while at late times ($t \gg 1$) they grow linearly $L \sim t$. The total lateral dissolution of CO_2 in the early advection dominated regime scales as $t^{3/2}$. The transition between the early time regime and the intermediate, diffusion dominated regime occurs as the increase in the surface area drives increasing dissolution. The transition from the intermediate diffusion dominated regime to the late-time advection dominated regime is due to CO_2 saturation of water in the low permeability layers which dampens diffusion over the more proximal parts of the CO_2 layers. The system tends to a steady state with a constant length zone at the front of the CO_2 finger in which dissolution of CO_2

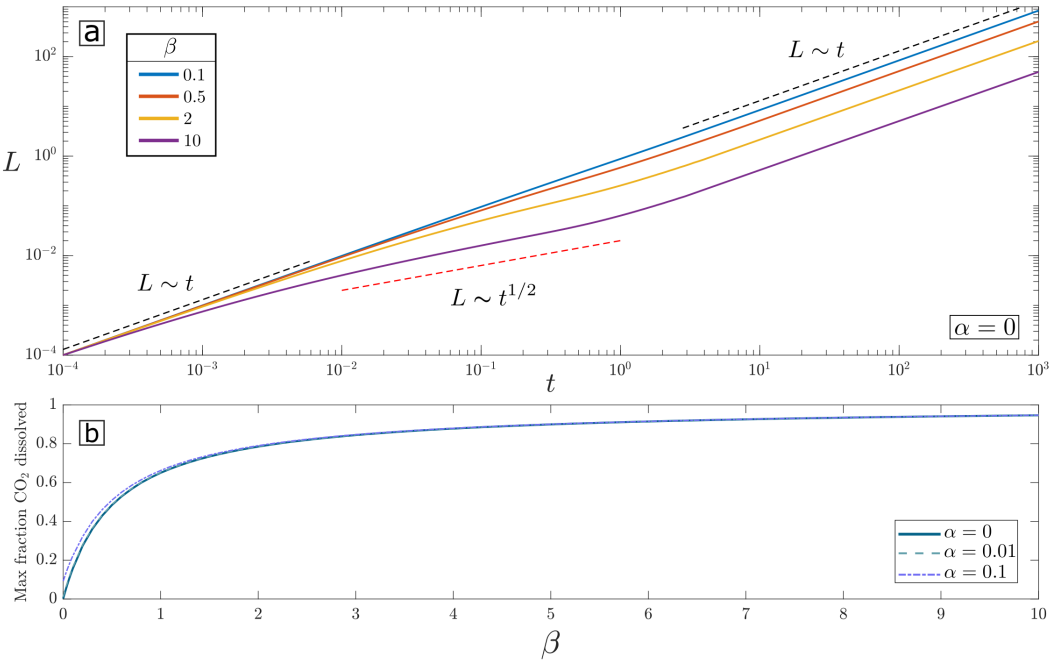

Figure 5. (a) The length of the CO_2 fingers plotted as a function of time for four different values of β. Also plotted is the line L (black dashed line), and the line $L^{1/2}$ (red dashed line). Larger values of β evolve with $L \sim t^{1/2}$ for longer before transitioning back to evolving with $L \sim t$. (b) The maximum fraction of injected CO_2 dissolved at steady state is plotted as a function of β for $\alpha = 0$, 0.01, 0.1.

is significant. The total dissolution scales proportionally with time in this late time regime (see supplementary material for graph of dissolution scaling). Figure 4b shows the fractional loss of CO_2 by dissolution as a function of time. At late times the fractional loss of CO_2 tends to a constant value which is less than one.

The value of β ($= h\phi_a c_0 / w\phi s_{nw}$) determines the transition time between the three regimes, where β is a ratio between the volume available for CO_2 to dissolve into the low permeability layers ($h\phi_a c_0$) and the volume of CO_2 in the high permeability layers ($w\phi s_{nw}$). Larger values of β allow more CO_2 diffusion leading to later transition to the late-time advection dominated regime (Figure 5a). Importantly, β also determines the maximum fraction of CO_2 dissolved at long times, reflecting the ratio of the volume of water available for saturation with CO_2 and the volume of CO_2 in the high permeability layers (Figure 5b).

4 Discussion

Evaluating the model using parameters appropriate to field settings establishes a practical sense of the permeability structures, lengths and timescales for which significant dissolution of CO_2 will occur. The Salt Creek Oil Field in Wyoming has been the site of CO_2 injection for enhanced oil recovery since 2004. In 2010, there was a monitored injection of CO_2 into a 20 m interval of the second Wall Creek sandstone unit. This is a highly heterogeneous deltaic sequence made up of mudstones, siltstones and sandstones in coarsening up sequences (Lee et al., 2005).

Bickle et al. (2017) estimated the permeability profile of the injection interval using porosity measurements calculated from gamma ray density logs. Order of magnitude permeability variations were found on ~ 0.5 m lengthscales. However, the resolution of the permeability distribution was limited by the resolution of the gamma ray density logs, which was ~ 0.35 m, and it is probable that large variations in permeability on smaller length scales exist.

The periodically repeating layered model is evaluated using parameters from the CO_2 injection into the second Wall Creek sandstone unit. The parameters used in the calculation are effective diffusivity $D = 2 \times 10^{-11}$ m^{2}s^{-1} using $D_m = 2 \times 10^{-9}$ m^{2}s^{-1} (Cadogan et al., 2014), $\phi_a = 0.12$ and $\tau = 5$, CO_2 input velocity $v_0 = 4 \times 10^{-5}$ ms^{-1} and porosity $\phi = 0.2$ (Bickle et al., 2017), fraction of the porosity occupied by CO_2 $s_{nw} = 0.8$ (Krevor et al., 2012), maximum saturation concentration $c_0 = 5.5$ wt% calculated at 15 Mpa, 50°C and a salinity of 0.05 mol NaCl/kg(H_2O) (Dubacq et al., 2013), and a high permeability layer spacing to thickness ratio $h/w = 1.5$ (Bickle et al., 2017). Three different widths for the high permeability layer have been plotted. These are $w = 0.5$ m, as calculated by (Bickle et al., 2017), as well as $w = 0.1$ m and $w = 0.05$ m, accounting for the limited resolution of the permeability distribution.

Figure 6a shows the length of the CO_2 finger from the injection point as a function of time. A separate curve is plotted for each value of w, with the ratio between high permeability layer spacing to layer width held constant. The length of the finger if no diffusive loss occurs is also plotted (black dashed line). As the width of the high permeability layer decreases, i.e., thinner and more finely spaced bedding, the distance the CO_2 propagates into the reservoir in a given time decreases becoming more pronounced at later times. When $w = 0.05$ m, the CO_2 travels around 10% less far than if no dissolution had occurred.

It is also useful to know how much of the injected CO_2 dissolves into the surrounding water. Figure 6b shows the fraction of the total injected CO_2 that has dissolved into the surrounding water as a function of time. The high permeability layers of width 0.1 m and 0.05 m show total dissolution of around 5% and 9% of the total injection volume respectively within the first two years of injection. Less CO_2 dissolves if bedded layers are thicker.

5 Conclusion

Injecting CO_2 into saline reservoirs with interbedded high and low permeability layers substantially enhances dissolution rates. As the fluid travels further into the reservoir, the increase in surface area between the CO_2 and surrounding water causes increased diffusive loss. The velocity at which CO_2 travels in the reservoir is dominated by the advective input flux at early times and transitions to an intermediate diffusion dominated regime as diffusive loss increases. At late times, the water in the low permeability layers reaches CO_2 saturation, dampening diffusion and resulting in a return to an advection dominated regime. The transition times between these regimes is governed by the ratio between the volume available for CO_2 dissolution in the low permeability layers and the volume of CO_2 within the high permeability layers. This ratio also governs the maximum fraction of injected CO_2 dissolved at late times. In reservoirs with characteristic bedding thicknesses of $\sim$0.1 m, the modelling implies that a significant fraction of the CO_2 will dissolve in water within a few years of injection. The tendency of low viscosity supercritical CO_2 to finger and the much more complex flow paths in real reservoirs will likely increase CO_2 dissolution rates above the minimum estimates from this model.

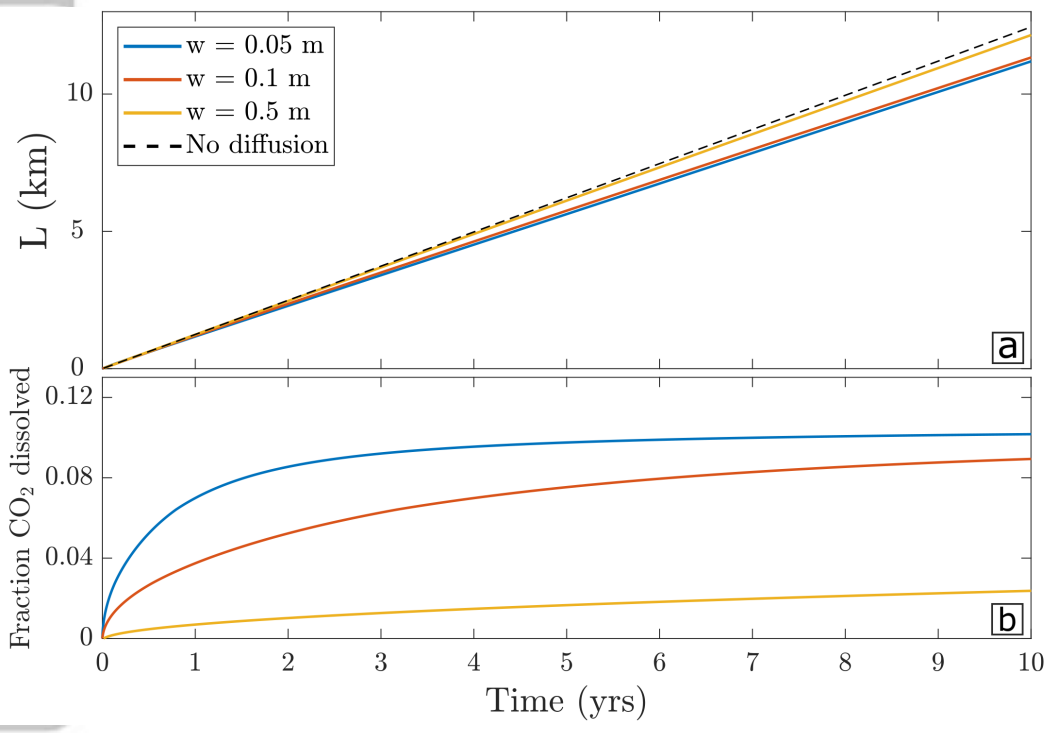

Figure 6. (a) Length of the CO_2 finger as a function of time for three high permeability channel widths (solid lines) and the length of the finger if no diffusive loss of CO_2 occurs (black dashed line). (b) The fraction of CO_2 dissolved as a function of time for three high permeability channel widths, w = 0.05, 0.1, 0.5 m. Values calculated using parameters from the Salt Creek field.

Acknowledgments

K.G. was funded by an Industrial CASE studentship from EPSRC and Shell (Grant No. EP/P510440/1). The authors would like to thank Thomasina Ball and Adam Butler for their helpful discussions. We would also like to thank Dylan Harp and Susan Hovorka for their constructive feedback. This research is a contribution from the GeoCquest consortium, a BHP-supported collaborative project between Cambridge, Stanford and Melbourne Universities and supported by funding from a NERC Highlights grant (Grant No. NE/N016084/1). The data from numerical simulations in this study are in the repository (https://doi.org/10.17863/CAM.47888) and will be made publicly available after publication.

References

Bickle, M., & Kampman, N. (2013). Lessons in carbon storage from geological analogues. *Geology*, *41*(4), 525–526. doi: 10.1130/focus0420132.1

Bickle, M., Kampman, N., Chapman, H., Ballentine, C., Dubacq, B., Galy, A., ... Zhou, Z. (2017). Rapid reactions between CO_2, brine and silicate minerals during geological carbon storage: Modelling based on a field CO_2 injection experiment. *Chemical Geology*, *468*(July), 17–31.

Cadogan, S. P., Maitland, C., & Trusler, J. P. M. (2014). Diffusion coefficients of CO_2 and N_2 in water at temperatures between 298.15 K and 423.15 K at pressures up to 45 MPa. *Journal of Chemical and Engineering data*, *59*, 519–525.

Carslaw, H. S., & Jaeger, J. (1959). *Conduction of heat in solids* (2nd ed. ed.). Oxford: Clarendon.

Dubacq, B., Bickle, M. J., & Evans, K. A. (2013). An activity model for phase equilibria in the H_2O-CO_2–NaCl system. *Geochemistry, Geophysics, Geosystems*, *110*, 229–252.

Ennis-King, J., & Paterson, L. (2005). Role of convective mixing in the long-term storage of carbon dioxide in deep saline formations. *Society of Petroleum Engineers Journal*, *10*(3), 350–356.

Freifeld, B. M., Trautz, R. C., Kharaka, Y. K., Phelps, T. J., Myer, L. R., Hovorka, S. D., & Collins, D. J. (2005). The U-tube: A novel system for acquiring borehole fluid samples from a deep geologic CO_2 sequestration experiment. *Journal of Geophysical Research*, *110*, 1–10. doi: 10.1029/2005JB003735

Gilfillan, S. M., Lollar, B. S., Holland, G., Blagburn, D., Stevens, S., Schoell, M., ... Ballentine, C. J. (2009). Solubility trapping in formation water as dominant CO_2 sink in natural gas fields. *Nature*, *458*(7238), 614–618. doi: 10.1038/nature07852

Green, C. P., & Ennis-King, J. (2014). Steady dissolution rate due to convective mixing in anisotropic porous media. *Advances in Water Resources*, *73*, 65–73. doi: 10.1016/j.advwatres.2014.07.002

Intergovernmental Panel on Climate Change. (2018). *Global Warming of 1.5C: An IPCC Special Report on the Impacts of Global Warming of 1.5C Above Pre-industrial levels and Related Global Greenhouse Gas Emissions Pathways, in the Context of Strengthening the Global Response to the Threat of Climate Change, Sustainable Development, and Efforts to Eradicate Poverty.* (Tech. Rep.).

Krevor, S., Blunt, M. J., Benson, S. M., Pentland, C. H., Reynolds, C., Al-Menhali, A., & Niu, B. (2015). Capillary trapping for geologic carbon dioxide storage – from pore scale physics to field scale implications. *International Journal of Greenhouse Gas Control*, *40*, 221–237.

Krevor, S., Pini, R., Zuo, L., & Benson, S. M. (2012). Relative permeability and trapping of CO_2 and water in sandstone rocks at reservoir conditions. *Water Resources Research*, *48*, 1–16.

LaForce, T., Ennis-King, J., Boreham, C., & Paterson, L. (2014). Residual CO_2

saturation estimate using noble gas tracers in a single-well field test: The CO2CRC Otway project. *International Journal of Greenhouse Gas Control*, *26*, 9–21. doi: 10.1016/j.ijggc.2014.04.009

Lee, K., Zeng, X., McMechan, G. A., Howell Jr, C. D., Bhattacharya, J. P., Marcy, F., & Olariu, C. (2005). A ground-penetrating radar survey of a delta-front reservoir analog in the Wall Creek member, Frontier Formation, Wyoming. *The American Association of Petroleum Geologists Bulletin*, *89*(9), 1139–1155.

Lindeberg, E., & Wessel-Berg, D. (1997). Vertical convection in an aquifer column under a gas cap of CO_2. *Energy Conversion and Management*, *38*, 229–234.

Lu, J., Cook, P. J., Hosseini, S. A., Yang, C., Romanak, K. D., Zhang, T., ... Hovorka, S. D. (2012). Complex fluid flow revealed by monitoring CO_2 injection in a fluvial formation. *Journal of Geophysical Research*, *117*(B03208). doi: 10.1029/2011JB008939

Michael, K., Golab, A., Shulakova, V., Ennis-King, J., Allinson, G., Sharma, S., & Aiken, T. (2010). Geological storage of CO_2 in saline aquifers — a review of the experience from existing storage operations. *International Journal of Greenhouse Gas Control*, *4*(4), 659–667.

Neufeld, J. A., Hesse, M. A., Riaz, A., Hallworth, M. A., Tchelepi, H. A., & Huppert, H. E. (2010). Convective dissolution of carbon dioxide in saline aquifers. *Geophysical Research Letters*, *37*(22), 2–6.

Pismen, L. M. (1974). Diffusion in porous media of a random structure. *Chemical Engineering Science*, *29*, 1227–1236.

Saffman, P. G., & Taylor, G. (1958). The penetration of a fluid into a porous medium or Hele-Shaw cell containing a more viscous liquid. *Proceedings of the Royal Society A*, *245*(1242), 312–329.

Sathaye, K. J., Hesse, M. A., Cassidy, M., & Stockli, D. F. (2014). Constraints on the magnitude and rate of CO_2 dissolution at Bravo Dome natural gas field. *Proceedings of the National Academy of Sciences*, *111*(43), 15332–15337.

Teng, H., & Yamasaki, A. (1998). Solubility of liquid CO_2 in synthetic sea water at temperatures from 278 K to 293 K and pressures from 6.44 MPa to 29.49 MPa, and densities of the corresponding aqueous solutions. *Journal of Chemical and Engineering Data*, *43*(1), 2–5.